Verifying multipartite entangled Greenberger-Horne-Zeilinger states via multiple quantum coherences

Ken X. Wei, Isaac Lauer, Srikanth Srinivasan, Neereja Sundaresan, Douglas T. McClure, David Toyli, David C. McKay, Jay M. Gambetta, and Sarah Sheldon

Phys. Rev. A **101**, 032343 — Published 25 March 2020

DOI: 10.1103/PhysRevA.101.032343

Verifying Multipartite Entangled GHZ States via Multiple Quantum Coherences

Ken X. Wei,* Isaac Lauer, Srikanth Srinivasan, Neereja Sundaresan, Douglas T. McClure, David Toyli, David C. McKay, Jay M. Gambetta, and Sarah Sheldon
IBM T.J. Watson Research Center, Yorktown Heights, NY 10598, USA
(Dated: February 28, 2020)

The ability to generate and verify multipartite entanglement is an important benchmark for near-term quantum devices. We develop a scalable entanglement metric based on multiple quantum coherences, and demonstrate experimentally on a 20-qubit superconducting device. We report a state fidelity of 0.5165 ± 0.0036 for an 18-qubit GHZ state, indicating multipartite entanglement across all 18 qubits. Our entanglement metric is robust to noise and only requires measuring the population in the ground state; it can be readily applied to other quantum devices to verify multipartite entanglement.

Universal quantum computers promise to solve many problems that are intractable classically [1, 2], but achieving fault tolerance will require a number of resources that are unavailable today. Until we can implement error correction, quantum systems will be beset with a certain amount of noise. Understanding how to best benchmark these near-term quantum devices is an active question [3]. Traditionally, the field has relied on local metrics such as one- and two-qubit gate fidelities since these are experimentally feasible even with full tomographic methods [4–7]. However, it has become increasingly clear that such local metrics do not capture the full intricacies of a multi-qubit device. Therefore, a number of multi-qubit metrics such as direct fidelity estimation [8, 9], three qubit simultaneous randomized benchmarking (RB) [10], direct RB [11], and quantum volume [12] have been proposed and measured. Another powerful multi-qubit metric is that of entanglement, specifically, measuring the largest possible multipartite entangled state on a device [13, 14]. Not only is the ability to generate entanglement indicative of high fidelity gate operations and qubit coherence, entangled states are the cornerstone of quantum speedups and they can be direct resources for quantum computing [15, 16]. Multipartite entanglement in Greenberger-Horne-Zeilinger (GHZ) states have been demonstrated with 10 superconducting circuits [17], 14 trapped ions [18], and 18 photons [19]. Recently, multipartite entanglement in a 12-qubit linear graph state and 18-qubit GHZ state were verified in superconducting qubit architectures [20, 21], as well as 20-qubit GHZ state in a Rydberg atoms array [22].

Here we generate and verify an 18-qubit entangled GHZ state on a 20-qubit superconducting device. Our entanglement metric is inspired by quantum sensing [23] and can be used to directly bound the state fidelity. The device is comprised of 20 fixed frequency transmon qubits, and implements two-qubit gates based on cross-resonance driving [24–26]. The device layout and the two qubit errors are shown in FIG. 1.

We verify the generation of GHZ states by measuring multiple quantum coherences (MQC) [29], a tool traditionally used in solid state NMR and more recently in trapped ions to study many-body correlations and quantum information scrambling [30, 31]. The experimental method to measure MQC has a strong overlap with quantum sensing and entanglement assisted metrology [32]. In the prototypical quantum sensing circuit shown in FIG. 2**A**, a GHZ state is used to sense static magnetic fields with Heisenberg-limited sensitivity; it works by taking advantage of an ideal GHZ state's amplified sensitiv-

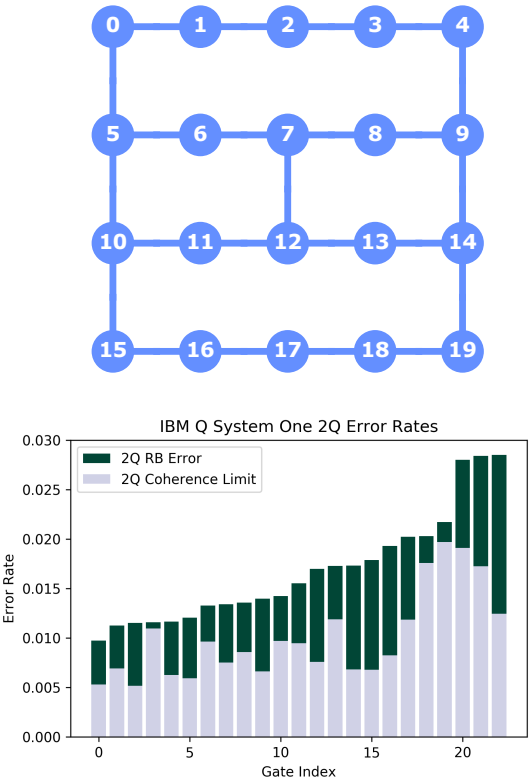

FIG. 1. **System One device layout and 2Q errors** Top: 20 qubit device layout and connectivity on IBM Q System One. Bottom: Comparison between 2Q error and 2Q coherence limit for all two-qubit gates on the device. The coherence properties of the device can be found in [27] and Appendix A.

* xkwei@ibm.com

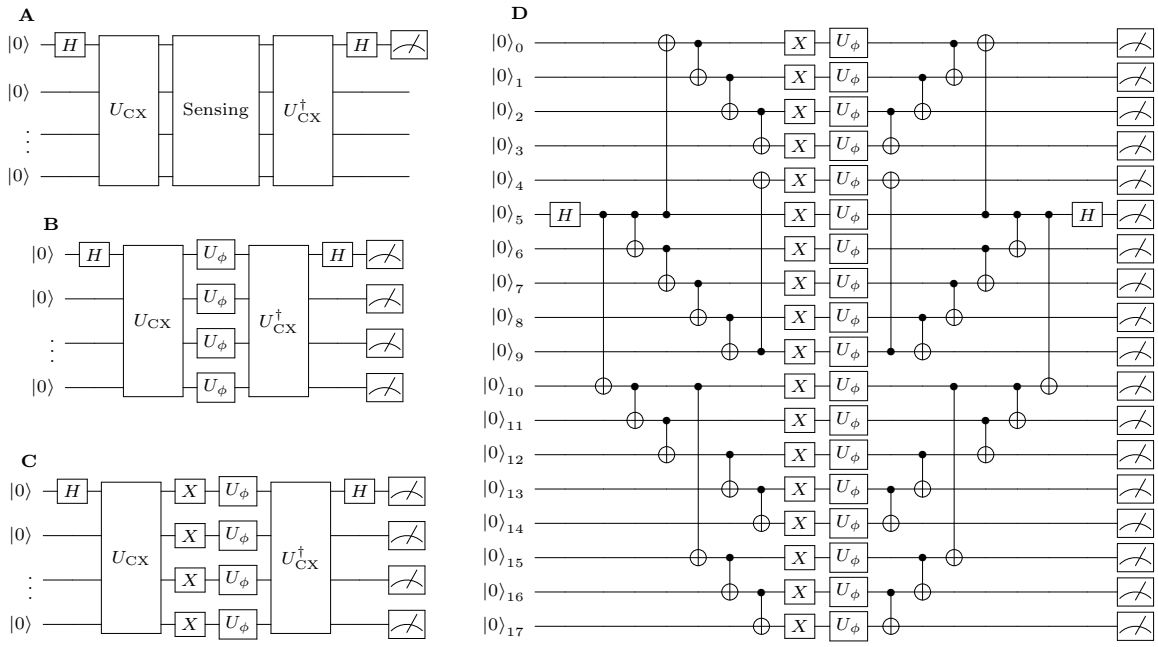

FIG. 2. **Quantum circuits A**: quantum sensing circuit. An ideal GHZ state is generated and used to sense an external magnetic field. After sensing, the GHZ state is disentangled and information about the magnetic field is encoded as a phase on the first qubit. **B**: MQC quantum circuit. Instead of sensing, we apply a collective rotation given by the unitary operator $U_\phi = e^{-i\phi/2\sum_j \sigma_z^j}$. We can implement this rotation instantaneously in our device by phase-shifting all subsequent pulses [28]. In the readout step, all qubits are measured to obtain the probability of system returning to initial state. **C**: refocused MQC quantum circuit. Similar to MQC except for the addition of a collective π-pulse on all qubits before U_ϕ. The π-pulse is used to reduce noise without affecting the GHZ state. **D**: experimental circuit for the 18-qubit MQC experiment on IBM Q System One.

ity to phase rotations of each of the individual qubits in the entangled state [23, 33–35]. If each qubit has a phase rotation of ϕ, then the N-qubit GHZ state rotates collectively by $N\phi$. By observing how sensitive a nonideal GHZ state responds to rotations, we can deduce how much entanglement is present in the state. The quantum circuit for measuring MQC is illustrated in FIG. 2**B**, and it can be described in four steps:

1. Starting from the N-qubit ground state: $|\text{GS}\rangle = |000..00\rangle$, apply a Hadamard gate on qubit 0 followed by a sequence of CX gates given by the unitary U_{CX}. Ideally this brings the system into the GHZ state: $|\text{GHZ}\rangle = \frac{1}{\sqrt{2}}(|000..00\rangle + |111..11\rangle)$

2. Apply a collective rotation given by the unitary U_ϕ on all qubits. This amounts to adding a phase $N\phi$ to the GHZ state: $\frac{1}{\sqrt{2}}(|000..00\rangle + e^{-iN\phi}\,|111..11\rangle)$

3. Disentangle the GHZ state by performing the CX gate sequence in reverse order. The amplified phase is mapped onto qubit 0: $\frac{1}{\sqrt{2}}(|0\rangle + e^{-iN\phi}\,|1\rangle) \otimes |00..00\rangle$

4. Read out the amplified phase by measuring the probability of the system returning to its initial state: $|\text{GS}\rangle$

In the absence of decoherence, the measured signal of this protocol is given by

$$\begin{aligned} S_\phi &= \langle \text{GS}|\rho_\text{f}|\text{GS}\rangle = |\,\langle 000..00|\,U_{\text{exp}}^\dagger U_\phi U_{\text{exp}}\,|000..00\rangle\,|^2 \\ &= \text{Tr}(\rho_\phi \rho) \end{aligned} \tag{1}$$

where ρ_f is the final state before measurement, $\rho = U_{\text{exp}}\,|\text{GS}\rangle\langle\text{GS}|\,U_{\text{exp}}^\dagger$, and $\rho_\phi = U_\phi \rho U_\phi^\dagger$. In the last step we used the cyclic property of the trace. It has been shown that Eq. (1) is still valid under general types of noise [36]. For an ideal GHZ state ($U_{\text{exp}} = U_{\text{GHZ}} = U_{\text{CX}} H_0$) Eq. (1) reduces to

$$S_\phi^{\text{ideal}} = \frac{1}{2}(1 + \cos(N\phi))$$

which can also be obtained by measuring the state $|0\rangle$ on qubit 0 in the final step. Since S_ϕ comes from the overlap between a rotated and unrotated density matrix, in the final step of the protocol the probability of all qubits being in the zero state must be measured. The constant term in S^{ideal} comes from the diagonal elements of the GHZ density matrix, whereas the oscillating term comes from the off-diagonal corner elements. Any difference between S_ϕ and S_ϕ^{ideal} is an indication that our GHZ state is imperfect. To quantify the state fidelity we focus on the MQC amplitudes, defined as the discrete Fourier

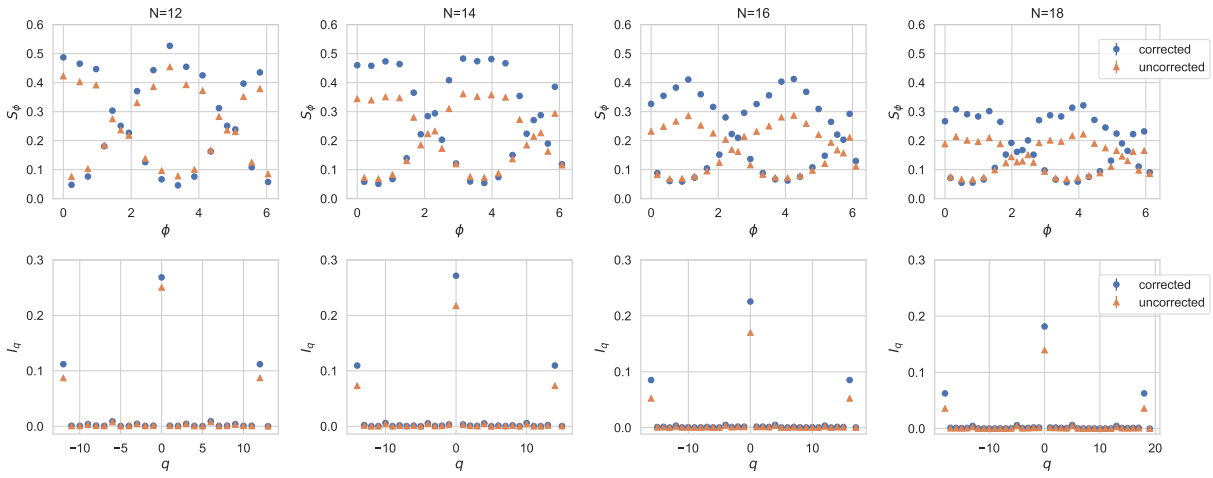

FIG. 3. **Experimentally measured S_ϕ and extracted MQC amplitudes** Top row: experimentally measured S_ϕ for $N = 12, 14, 16, 18$. Bottom row: corresponding MQC amplitudes extracted by discrete Fourier transforming S_ϕ. The errorbar corresponds to one standard error linearly propagated from uncertainties in S_ϕ.

transform of S_ϕ:

$$I_q = \mathcal{N}^{-1} |\sum_\phi e^{iq\phi} S_\phi| \tag{2}$$

where $\mathcal{N}$ is a normalization factor. The experimentally prepared GHZ state can have a phase error in the form of $|\text{GHZ}(\phi_\epsilon)\rangle \frac{1}{\sqrt{2}}(|000..00\rangle + e^{i\phi_\epsilon}|111..11\rangle)$. I_q defined in Eq. (2) is insensitive to the phase error ϕ_ϵ; one can determine ϕ_ϵ by analyzing the real and imaginary parts of $\sum_\phi e^{iq\phi} S_\phi$, as shown in Appendix E. The maximum N-qubit GHZ state fidelity defined as $F = \max_{\phi_\epsilon} \langle \text{GHZ}(\phi_\epsilon)|\rho|\text{GHZ}(\phi_\epsilon)\rangle$ can be bounded by

$$2\sqrt{I_N} \leq F \leq \sqrt{I_0/2} + \sqrt{I_N} \tag{3}$$

For a perfect GHZ state we have $I_0 = 2I_N = 1/2$, and all other I_q being zero. We can also directly obtain the state fidelity as $F = \frac{1}{2}(P_{000..00} + P_{111..11}) + \sqrt{I_N}$, where $P_{000..00}$ and $P_{111..11}$ are the populations of $|000..00\rangle$ and $|111..11\rangle$ in the density matrix. A discussion on MQC amplitudes and proof of Eq. (3) are given in Appendix B and C. For a N-qubit state to have multipartite GHZ entanglement, it needs to have a minimal fidelity of 0.5 [37, 38]. Eq. (1) and Eq. (3) are valid under common types of noise. In Appendix C we show they are valid in simulations taking into account T_1/T_2 noises, CNOT gate error, and ZZ interactions.

This method can be seen as complementary to parity oscillation measurements commonly used in trapped ions to verify GHZ entanglement [18, 39, 40], MQC offers two main benefits: robustness to noise and scalability in readout correction. Parity oscillations measure the expectation value $\langle \text{GHZ}_\phi|ZZZ...ZZ|\text{GHZ}_\phi\rangle$ as a function of ϕ, where $|\text{GHZ}_\phi\rangle = \otimes_j^N e^{\frac{i\pi}{4}(\cos\phi\sigma_x^j + \sin\phi\sigma_y^j)}|\text{GHZ}\rangle$ [18]. The amplitude of the parity oscillations gives coherence $C = |\rho_{000..00,111..11}| + |\rho_{111..11,000..00}|$, where $\rho_{000..00,111..11}$ is the off-diagonal element in the density matrix. C is related to the fidelity via $F = \frac{1}{2}(P_{000..00} + P_{111..11} + C)$ [18]. The coherence is related to MQC amplitudes via $C = 2\sqrt{I_N}$. At first our entanglement metric appears disadvantageous compared to parity oscillations since it takes twice the circuit length. However our experiments can be made robust against noise. Just as a Hahn echo refocuses low frequency noise and reduces dephasing [41], adding a π-pulse after making the GHZ state can dramatically improve the measured fidelity. The quantum circuit for refocused MQC is illustrated in FIG. 2**C**. We find experimentally the 20-qubit state fidelity to increase by nearly 11% by adding the refocusing π-pulse, as shown in FIG. 4**B**. In addition, our entanglement metric only requires measurement of the initial state.

In addition to accommodating dynamical decoupling techniques, the MQC method is also less sensitive to readout errors. We point out that parity oscillations in GHZ states have been measured previously on the IBM Q 16-qubit device [42] with average readout error of 7%, but multipartite entanglement cannot be established beyond five qubits. Aside from control imperfections and decoherence, readout errors limit our ability to measure the entangled state, even though the state itself can be highly entangled. Since readout errors are independent from entanglement we can calibrate them out of the measurement. Here we implement a scalable readout mitigation method based on constructing a truncated calibration matrix, the details are explained in Appendix F.

We have experimentally generated GHZ states for $N = 11$ to $N = 20$, and measured S_ϕ in Eq. (1) and extracted the corresponding MQC amplitudes. The data for 12, 14, 16, and 18-qubit GHZ states are shown in FIG. 3, and the circuit used in the 18-qubit experiment is shown in FIG. 2**D**. For each N, we measure S_ϕ for $\phi = \frac{\pi j}{N+1}$, where $j = 0, 1, 2, \cdots, 2N+1$ so the highest frequency detectable is $N + 1$. The result of each experiment is averaged

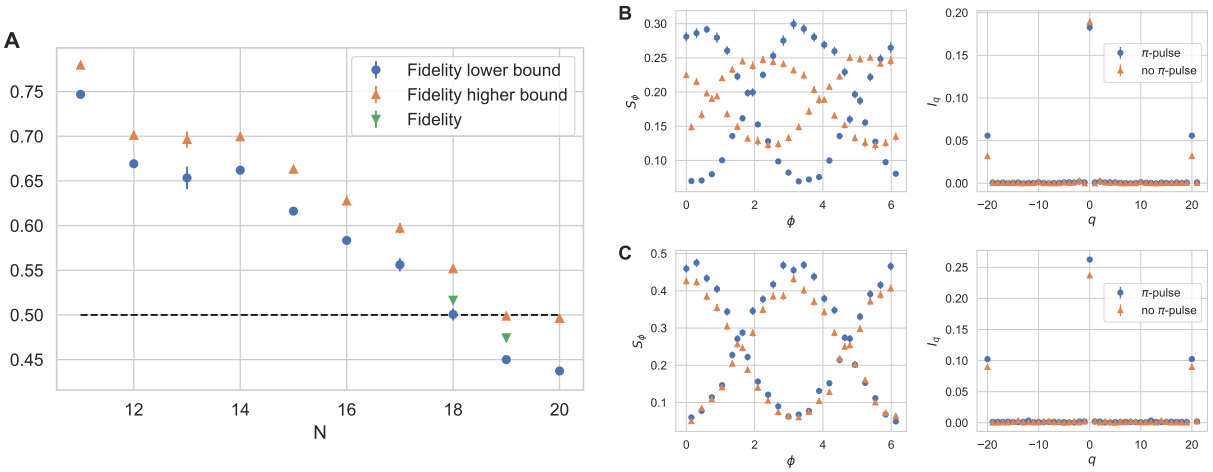

FIG. 4. **Fidelity bounds and 20q data A**: experimentally extracted fidelity bounds according to Eq. (3) for $N = 11$ to $N = 20$ with readout correction. Error bars corresponds to linearly propagated uncertainties in the corresponding S_ϕ. For $N = 18$ and $N = 19$ the fidelities are also presented. **B**: experimentally measured 20-qubit S_ϕ and MQC amplitudes with and without the refocusing π-pulse. **C**: simulated results using basic noise model described in [43]

.

over 16384 shots, and the errorbar corresponds to one standard error obtained from eight experiments. There is considerable difference between the results with and without readout correction. Here the calibration matrix is constructed using 256 basis states (see Appendix F), and each basis state measurement is averaged over 4096 shots.

From the experimentally extracted MQC amplitudes shown in the bottom row of FIG. 3, we see one peak located at $q = 0$ and two peaks at $q = \pm N$, characteristic of N-qubit GHZ states. Peak amplitudes become lower with increasing N, indicating larger N-qubit GHZ states have lower fidelities. Using Eq. (3) we extract the upper and lower bounds on state fidelities with readout calibrations as a function of N, as shown in FIG. 4**A**. For $N = 11$ to $N = 17$ the fidelity lower bound is clearly higher than the 0.5 threshold for multipartite entanglement. For $N = 18$ the lower bound is 0.5006 ± 0.0067, in this case we measure $P_{000..00}$ and $P_{111..11}$ for the GHZ state in addition to MQC amplitudes to obtain the state fidelity of $F = 0.5165 \pm 0.0036$, confirming that the 18-qubit GHZ state is multipartite entangled. We have not been able to establish multipartite entanglement with 19 and 20-qubit GHZ states. Without applying the aforementioned readout calibration, the highest number of multipartite entangled qubits we can measure is $N = 14$ with a fidelity lower bound of 0.5406 ± 0.0037. We compare fidelities extracted from our method with that from quantum state tomography (QST) [44] for small GHZ states, the results are summarized in Table I. While the MQC method appears to give slightly higher state fidelity, we expect these results are within the errors of the tomography experiments. Each experiment is averaged over 16384 shots and readout corrected. Our method to experimentally quantify multipartite entanglement for GHZ states can be applied to other states that are locally equivalent to GHZ states, such as star graph and complete graph states [45]. The only difference is in the rotation step. For star graph states, instead of applying U_ϕ on all qubits, apply U_ϕ on the central qubit and $HU_\phi H$ on the rest. For complete graph states, apply $e^{-\frac{i\pi}{4}\sigma_x} U_\phi e^{\frac{i\pi}{4}\sigma_x}$ on all qubits.

TABLE I. **Fidelity Comparison for small GHZ states**

Method	2q GHZ	3q GHZ	4q GHZ	5q GHZ
QST	0.96	0.93	0.87	0.85
MQC	0.98	0.94	0.87	0.86

There are several experimental limitations to entangling large GHZ states in our device. First, the circuit depth required to generate a N-qubit GHZ state scales as $\mathcal{O}(N)$; in contrast with the linear graph state, where only two steps are needed independent of N [14, 20]. This makes GHZ states particularly fragile to decoherence. We choose an entangling path on our device that takes the least amount of time to complete; the physical qubits involved for each N are listed in Appendix A. Second, there are instances where CX gates, implemented by cross-resonance driving, are run on adjacent qubit pairs. Simultaneous adjacent CX gates will have lower fidelity than individual CX gates due to always-on ZZ interactions and cross-driving effects between neighboring qubits. Third, since the CX gates are applied sequentially, there will inevitably be free evolution on idle qubits leading to unitary errors. In addition, due to pulse alignment restrictions in the software, the entangling and the disentangling operations take different times to complete, making the π-pulse not as effective as it can be.

This might explain why the measured S_ϕ appears phase-shifted.

We use a basic noise model built from device parameters to simulate the 20-qubit MQC experiments using Qiskit [43]. The simulation models one- and two-qubit gate errors as a depolarizing error plus a thermal relaxation error such that the total error equals the error measured experimentally from randomized benchmarking; the details of the basic noise model can be found in Qiskit tutorial [43]. To compare with experiments, we turn off readout error in the simulation and average over 2048 shots. The simulation shows higher fidelities than the experiment and does not appear to capture the effects of the refocusing π pulse, as shown in FIG. 4**C**. This suggests that the experimental system has slow drifts which can be refocused by π-pulses. Interestingly, it has been demonstrated that dynamical decoupling is remarkably effective at extending the lifetime of GHZ states [46].

We demonstrate in this work an experimentally scalable entanglement metric based on multiple quantum coherences, and applied it to verify 18-qubit multipartite GHZ entanglement. Our experiments show encouraging results in the ability to entangle and disentangle highly correlated many-body states in near term quantum devices. We are exploring new variations of CX gates which can be applied simultaneously on adjacent qubit pairs while canceling ZZ errors [47]. This should improve gate fidelity in the entangling and disentangling steps. The lifetimes of MQC amplitudes should be measured and compared to those of parity oscillations, which were reported to decrease as N^2 in trapped ions [18] and N in superconducting qubits [48]. It will be interesting to extend MQC to other entangled states such as the W-state and study their entanglement properties. Lastly, the newly developed error mitigation techniques [49, 50] may give us insights to the maximum GHZ fidelity achievable in our device in the limit of zero noise.

ACKNOWLEDGMENTS

We thank T. Alexander, L. Bishop, P. Cappellaro, J. M. Chow, A. Córcoles, P. Jurcevic, A. Kandala, J. Kim, K. Krsulich, E. Magesan, S. Merkel, A. Mezzacapo, Z. Minev, P. Nation, J. Smolin, M. Steffen, T. Scholten, M. Takita, K. Temme, and C. Wood for insightful discussions. This work was supported by ARO under Contract No. W911NF-14-1-0124. The authors declare that they have no competing interests.

Appendix A: Device Parameters

In Table II we show the typical qubit parameters for the device. In Table III we list the physical qubits involved in the state tomography experiments and the N-qubit MQC experiments on the device. The numbers labeling the physical qubits are shown in FIG. 1 in the main text.

TABLE II. **Qubit parameters on IBM System One** The qubit frequency, T_1, $T_{2,\text{echo}}$, readout fidelity are presented.

Qubit	Frequency (GHz)	T_1 (μs)	$T_{2,\text{echo}}$ (μs)	Readout Fidelity
Q0	4.666	88.1	76.6	98.1
Q1	4.760	69.0	75.7	96.4
Q2	4.609	58.3	65.4	97.2
Q3	5.031	60.9	73.0	79.7
Q4	4.657	69.1	78.1	96.6
Q5	4.752	74.4	71.9	95.9
Q6	4.829	60.2	65.8	98.1
Q7	4.698	80.7	79.5	96.4
Q8	4.893	64.0	75.7	96.5
Q9	4.731	63.3	70.7	93.0
Q10	4.840	59.1	62.9	96.6
Q11	4.755	64.1	56.3	97.8
Q12	4.621	85.4	87.2	96.6
Q13	4.859	69.4	83.2	93.6
Q14	4.394	101.6	86.6	93.5
Q15	4.693	76.1	74.3	98.1
Q16	4.512	70.3	80.1	95.0
Q17	4.719	66.4	79.2	97.8
Q18	4.321	73.6	80.7	93.0
Q19	4.593	83.3	85.5	97.6
Median	4.708	69.2	76.2	96.6

TABLE III. **Physical qubits used on IBM System One for state tomography and MQC experiments**

N	Physical qubits used
2	[5, 10]
3	[5, 10, 6]
4	[5, 10, 6, 11]
5	[5, 10, 6, 11, 0]
11	[5, 10, 6, 11, 0, 12, 7, 15, 1, 8, 13]
12	[5, 10, 6, 11, 0, 12, 7, 15, 1, 8, 13, 16]
13	[5, 10, 6, 11, 0, 12, 7, 15, 1, 8, 13, 16, 2]
14	[5, 10, 6, 11, 0, 12, 7, 15, 1, 8, 13, 16, 2, 9]
15	[5, 10, 6, 11, 0, 12, 7, 15, 1, 8, 13, 16, 2, 9, 17]
16	[5, 10, 6, 11, 0, 12, 7, 15, 1, 8, 13, 16, 2, 9, 17, 4]
17	[5, 10, 6, 11, 0, 12, 7, 15, 1, 8, 13, 16, 2, 9, 17, 4, 14]
18	[5, 10, 6, 11, 0, 12, 7, 15, 1, 8, 13, 16, 2, 9, 17, 4, 14, 3]
19	[5, 10, 6, 11, 0, 12, 7, 15, 1, 8, 13, 16, 2, 9, 17, 4, 14, 3, 18]
20	[5, 10, 6, 11, 0, 12, 7, 15, 1, 8, 13, 16, 2, 9, 17, 4, 14, 3, 18, 19]

Appendix B: Multiple Quantum Coherences

Consider writing the density matrix as $\rho = \sum_{m,m'} \rho_{m,m'} |m\rangle\langle m'|$, where the basis states satisfy $\sum_j \sigma_z^j/2 \, |m\rangle = m \, |m\rangle$. We can expand the density matrix as $\rho = \sum_q \rho_q$, where $\rho_q = \sum_m \rho_{m,m-q} \, |m\rangle\langle m-q|$.

It can be shown that ρ_q satisfies the following:

$$e^{-i\frac{\phi}{2}\sum_j \sigma_z^j}\rho_q e^{i\frac{\phi}{2}\sum_j \sigma_z^j} = e^{-iq\phi}\rho_q, \quad \left[\sum_j \sigma_z^j/2, \rho_q\right] = q\rho_q \tag{B1}$$

Since ρ is hermitian we also have $\rho_q^\dagger = \rho_{-q}$. Each ρ_q occupies a different part of the density matrix, and it obeys the orthogonality condition $\mathrm{Tr}(\rho_q\rho_p) = \delta_{q,-p}\mathrm{Tr}(\rho_q\rho_{-q})$. While each ρ_q is not directly observable, the trace $I_q = \mathrm{Tr}(\rho_q\rho_{-q})$ is. I_q is the multiple quantum coherence amplitude, and it can be found by Fourier transforming the overlap signal $S_\phi = \mathrm{Tr}(\rho_\phi\rho)$, where $\rho_\phi = e^{-i\frac{\phi}{2}\sum_j \sigma_z^j}\rho e^{i\frac{\phi}{2}\sum_j \sigma_z^j}$. For a general time-dependent density matrix, measuring S_ϕ requires the ability to implement time-reversed evolution. Upon expanding ρ inside S_ϕ and using the first relation in Eq. (B1) we have

$$\begin{aligned} S_\phi &= \mathrm{Tr}(\sum_q e^{-iq\phi}\rho_q \sum_p \rho_p) = \sum_q e^{-iq\phi}\mathrm{Tr}(\rho_q \sum_p \rho_p) \\ &= \sum_q e^{-iq\phi}\mathrm{Tr}(\rho_q\rho_{-q}) = \sum_q e^{-iq\phi} I_q \end{aligned}$$

where in the second to last step we used the orthogonality condition. Fourier transforming gives $I_q = \mathcal{N}^{-1}\sum_\phi e^{iq\phi}S_\phi$, where $\mathcal{N}$ is a normalization constant depending on the number of ϕ used in the experiments. If the maximum coherence order to be measured is $q_{\max}$, we need at least $2q_{\max}$ experiments. The angle ϕ can be chosen as $\phi = \frac{\pi j}{q_{\max}}$ where $j = 0, 1, 2, \cdots 2q_{\max} - 1$ and $\mathcal{N} = 2q_{\max}$. While our discussion assumes unitary evolution, it has been shown that in certain types of decoherence the experimental method for measuring multiple quantum coherence is still valid [36].

For an ideal N-qubit GHZ state, the nonzero elements in the density matrix resides only in the four corners. Therefore only three components arise in the expansion: $\rho^{\mathrm{GHZ}} = \rho_0^{\mathrm{GHZ}} + \rho_N^{\mathrm{GHZ}} + \rho_{-N}^{\mathrm{GHZ}}$. Explicitly they are given by

$$\begin{aligned} \rho_0^{\mathrm{GHZ}} &= \frac{1}{2}(|000..00\rangle\langle 000..00| + |111..11\rangle\langle 111..11|), \\ \rho_N^{\mathrm{GHZ}} &= \frac{1}{2}|000..00\rangle\langle 111..11|, \quad \rho_{-N}^{\mathrm{GHZ}} = \rho_N^{\mathrm{GHZ}\dagger} \end{aligned}$$

the corresponding multiple quantum amplitudes are given by

$$\begin{aligned} I_0^{\mathrm{GHZ}} &= \mathrm{Tr}(\rho_0^{\mathrm{GHZ}}\rho_0^{\mathrm{GHZ}}) = \frac{1}{2}, \\ I_N^{\mathrm{GHZ}} &= \mathrm{Tr}(\rho_N^{\mathrm{GHZ}}\rho_{-N}^{\mathrm{GHZ}}) = \frac{1}{4}, \quad I_{-N}^{\mathrm{GHZ}} = I_N^{\mathrm{GHZ}} \end{aligned} \tag{B2}$$

Multiple quantum coherence amplitudes are symmetric: $I_q = I_{-q}$.

Appendix C: Fidelity Bounds from MQC Amplitudes

The state fidelity, given by $F = \langle \mathrm{GHZ}|\rho|\mathrm{GHZ}\rangle = \mathrm{Tr}(\rho\rho^{\mathrm{GHZ}})$, can be bounded by:

$$2\sqrt{I_N} \le F \le \sqrt{I_0/2} + \sqrt{I_N} \tag{C1}$$

The upper bound on F follows from the Cauchy-Schwarz inequality:

$$\begin{aligned} \mathrm{Tr}(\rho\rho^{\mathrm{GHZ}}) &= \sum_{q=-N}^{N} \mathrm{Tr}(\rho_q\rho_{-q}^{\mathrm{GHZ}}) \\ &\le \sum_{q=-N}^{N} \sqrt{\mathrm{Tr}(\rho_q\rho_{-q})\mathrm{Tr}(\rho_q^{\mathrm{GHZ}}\rho_{-q}^{\mathrm{GHZ}})} = \sqrt{I_0/2} + \sqrt{I_N} \end{aligned}$$

To prove the lower bound we first notice that

$$\begin{aligned} F &= \mathrm{Tr}(\rho_0\rho_0^{\mathrm{GHZ}}) + \mathrm{Tr}(\rho_N\rho_{-N}^{\mathrm{GHZ}}) + \mathrm{Tr}(\rho_{-N}\rho_N^{\mathrm{GHZ}}) \\ &\ge 2(\mathrm{Tr}(\rho_N\rho_{-N}^{\mathrm{GHZ}}) + \mathrm{Tr}(\rho_{-N}\rho_N^{\mathrm{GHZ}})) \end{aligned} \tag{C2}$$

This can be proved by writing the density matrix as $\rho = \sum_j w_j |\psi_j\rangle\langle\psi_j|$, where $w_j \ge 0$ and $\sum_j w_j = 1$. The state vectors $|\psi_j\rangle$ need not to be orthogonal, we can in general expand $|\psi_j\rangle$ as

$$|\psi_j\rangle = \alpha_j |00...0000\rangle + \beta_j |11...1111\rangle + \cdots$$

Since $|\alpha_j - \beta_j|^2 \ge 0$, upon expanding we have $|\alpha_j|^2 + |\beta_j|^2 \ge \alpha_j\beta_j^* + \alpha_j^*\beta_j$. It then follows that

$$\frac{1}{2}\sum_j w_j(|\alpha_j|^2 + |\beta_j|^2) \ge \frac{1}{2}\sum_j w_j(\alpha_j\beta_j^* + \alpha_j^*\beta_j)$$

which is the same as

$$\mathrm{Tr}(\rho_0\rho_0^{\mathrm{GHZ}}) \ge \mathrm{Tr}(\rho_N\rho_{-N}^{\mathrm{GHZ}}) + \mathrm{Tr}(\rho_{-N}\rho_N^{\mathrm{GHZ}})$$

thereby proving Eq. (C2). One can go one step further by noting that $\rho_N = \kappa\rho_N^{\mathrm{GHZ}}$, where κ is a complex constant. Using $\mathrm{Tr}(\rho_N\rho_{-N}^{\mathrm{GHZ}}) = \kappa I_N^{\mathrm{GHZ}} = \frac{1}{\kappa^*}I_N$ we can show that $|\kappa| = 2\sqrt{I_N}$. Notice κ can always be made real by appropriately rotating the density matrix ρ. Substituting $\rho_N = 2\sqrt{I_N}\rho_N^{\mathrm{GHZ}}$ into Eq. (C2) gives $2\sqrt{I_N}$ as the lower bound of F. In addition to the fidelity bounds, we can also obtain the GHZ state fidelity F:

$$F = \frac{1}{2}(P_{000..00} + P_{111..11}) + \sqrt{I_N}$$

where $P_{000..00} = \langle 000...00|\rho|000...00\rangle$ and $P_{111..11} = \langle 111...11|\rho|111...11\rangle$ are the probabilities of finding all zeroes and all ones in the state ρ.

Appendix D: Numerical Simulations

Here we look at some numerical simulations of the multiple quantum coherence (MQC) technique outlined in

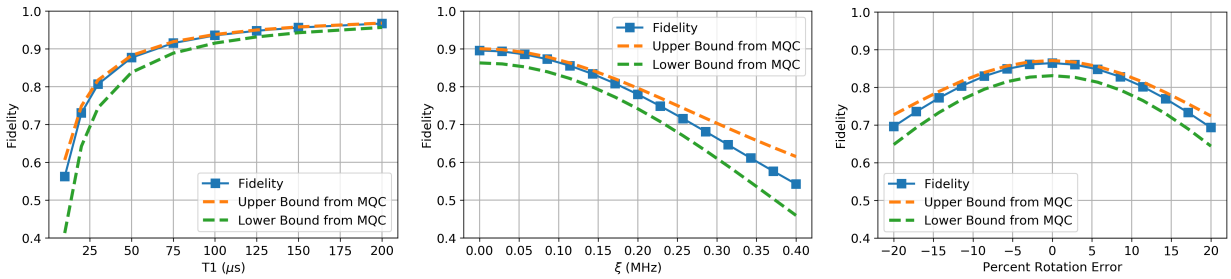

FIG. 5. **Simulated fidelity bounds** Left: Six-qubit GHZ state fidelity versus T_1 ($T_2 = T_1$) measured directly (solid blue line), and with the bounds from the MQC method. Middle: Six-qubit GHZ state fidelity versus the ZZ interaction between the qubits ($\xi|11\rangle\langle 11|$) measured directly (solid blue line), and with the bounds from the MQC method. Right: Six-qubit GHZ state fidelity versus the CNOT rotation error measured directly (solid blue line), and with the bounds from the MQC method. For all three errors the fidelity is correctly bounded according to Eq. C1.

the main paper. The simulation starts with a density matrix in the ground state (i.e. $\rho_0 = |00..00\rangle\langle 00..00|$). The circuit to be simulated is divided into n_g steps where each step corresponds to the time required to perform a single qubit gate operation; the two-qubit gates are split into m gates where m is the length ratio between the two-qubit and single-qubit gates (here $m = 5$). For each step s we apply discrete unitary operations for the gates at step s in the circuit followed by a coherent error map (additional unwanted unitary terms) and then a T_1, T_2 map. This is repeated for all n_g steps, carrying through the resulting density matrix. This technique is outlined in detail in the supplemental materials to Ref. [51]. To compare to the results of the experiment in the main paper, we first simulate the gates that create the GHZ state and calculate the state fidelity $\langle\Psi_{\text{ideal}}|\rho_{\text{sim}}|\Psi_{\text{ideal}}\rangle$ where $|\Psi_{\text{ideal}}\rangle = (|00\ldots0\rangle + e^{i\theta}|11\ldots1\rangle)/\sqrt{2}$ (we assume θ is set to optimize the fidelity). Next we apply the phase rotations ϕ to each qubit and unwind the GHZ state and measure the population in $|00\ldots0\rangle$ versus ϕ. As in the experiment, we do a Fourier transform to get the coherence peaks and determine the bound in Eq. C1. If the true fidelity lies within the bound then the technique is valid. For all the simulations we consider 6 qubits in a line where the CNOT gates are applied sequentially from one end to the other end. We assume the CNOT gates are 500 ns and the single qubit gates 100 ns, these values are consistent with actual device parameters.

In the following we consider T_1/T_2 noise, ZZ error and CNOT rotation error. In all cases the state fidelity lies within the bounds set by Eq. (C1).

1. T_1/T_2 Noise

First we consider the situation where the gates are perfect but there is T_1/T_2 noise. We assume $T_1 = T_2 = 60\mu$s and that all the qubits have the same T_1. The data is shown in the left of FIG. 5 as a function of T_1.

2. ZZ Error

Next we consider that there is a ZZ term in the Hamiltonian expressed as a term $H_{ZZ} = \xi|11\rangle\langle 11|$; the typical values measured in the device are on the order of tens of kilohertz. The ZZ term is present between all neighbors on the line (and between the first and last qubits, i.e. we assume a loop). For this simulation we leave $T_1 = T_2 = 60\mu$s. The data is shown in the middle of FIG. 5.

3. CNOT Error

Finally we consider that there is an over/under rotation error in the CNOT gate. We assume the true gate is $CR_X(\pi(1+\gamma))$, where CR_X is the cross resonance interaction aligned along the X-axis of the target qubit and $\gamma = 0$ corresponds to a CNOT. We look at the state fidelity as we vary γ. For this simulation we leave $T_1 = T_2 = 60\mu s$ and $\xi = 0.1$ MHz. The data is shown in the right of FIG. 5.

Appendix E: Extracting GHZ Phase from MQC

We describe how the phase of the GHZ state can be extracted from MQC experiments and compare with the phase extracted from quantum state tomography (QST) and parity oscillations. A rotated GHZ state acquires a relative phase and can be written as $|\text{GHZ}(\theta)\rangle = \frac{1}{\sqrt{2}}(|000..00\rangle + e^{i\theta}|111..11\rangle)$. By performing QST on the density matrix $\rho(\theta) = |\text{GHZ}(\theta)\rangle\langle\text{GHZ}(\theta)|$, the relative phase θ can be obtained as

$$\theta = -\arctan\left[\frac{\text{Im}(\rho_{000..00,111..11})}{\text{Re}(\rho_{000..00,111..11})}\right]$$

where $\rho_{000..00,111..11} = \langle 000..00|\rho(\theta)|111..11\rangle$, and the coherence is given by $C = 2|\rho_{000..00,111..11}|$. The phase θ can also be obtained from parity oscillations, which is

extracted from the following expectation value

$$P_\phi = \mathrm{Tr}(\rho_\theta \Pi_j (\cos\phi \sigma_x^j + \sin\phi \sigma_y^j)) \\ = \mathrm{Tr}(\rho_\theta \Pi_j (e^{-i\phi}\sigma_+^j + e^{i\phi}\sigma_-^j)) = C\cos(N\phi - \theta)$$

The measured P_ϕ can have other frequency components in addition to $N\phi$ due to experimental imperfections. Instead of fitting P_ϕ to a cosine function, we take the Fourier transform of P_ϕ: $J_q = \mathcal{N}^{-1}\sum_\phi e^{iq\phi}P_\phi$ and extract θ via

$$\theta = -\arctan\left[\frac{\mathrm{Im}(J_N)}{\mathrm{Re}(J_N)}\right]$$

The coherence is given by $C = |J_N| + |J_{-N}|$.

Finally we move on to MQC. The measured signal $S_\phi = \mathrm{Tr}(\rho_\phi \rho)$ can be written as $\mathrm{Tr}(\rho_\phi(\theta)\rho(-\theta'))$, where we allow for two possibly different phases θ and θ' due to experimental imperfections within the entangling and disentangling operations. The resulting signal is given by $S_\phi = \frac{1}{2}(1+\cos(N\phi+\theta+\theta'))$. Now consider MQC with spin echo in the middle, the signal becomes $S_\phi^\pi = \frac{1}{2}(1+\cos(N\phi-\theta+\theta'))$. Comparing the two expressions we can extract θ via

$$\theta = \frac{1}{2}\left(\arctan\left[\frac{\mathrm{Im}(I_N)}{\mathrm{Re}(I_N)}\right] - \arctan\left[\frac{\mathrm{Im}(I_N^\pi)}{\mathrm{Re}(I_N^\pi)}\right]\right)$$

where I_N^π and I_N correspond to the N-th MQC amplitudes obtained with and without the spin echo.

We compare the experimentally extracted θ from QST, parity oscillation, and MQC for a 4-qubit GHZ state. The GHZ state is generated using a linear sequence of CNOT gates acting on qubits 5, 10, 11, and 12. The extracted θ is similar across all three methods, as shown in FIG. 6**A**. Furthermore, we compare the extracted coherence C and observed similar values for all methods, as shown in FIG. 6**B**. The coherence obtained from MQC with spin echo is slightly higher than MQC without the echo, this difference can be attributed to dephasing.

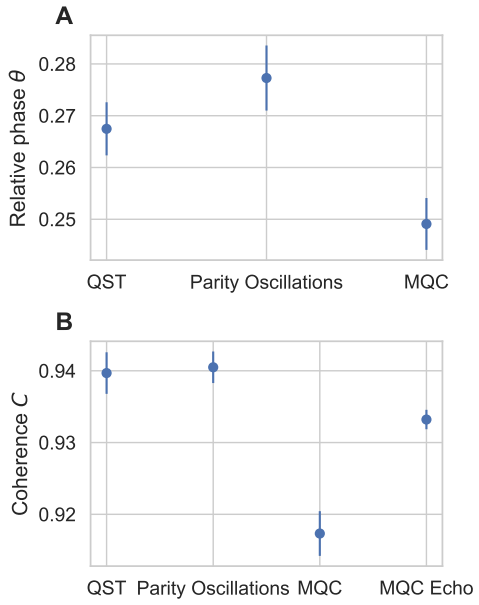

FIG. 6. **Extracting GHZ phase θ and coherence C A**: Extracted phase θ from QST, parity oscillations, and MQC for a 4-qubit GHZ state. The errorbar corresponds to one standard deviation of the mean obtained from eight runs of the same experiment, each experiment is readout corrected and uses 4096 shots. **B**: Extracted coherence C from QST, parity oscillations, MQC, and MQC with spin echo for a 4-qubit GHZ state.

Appendix F: Readout Calibration

To mitigate measurement errors, we experimentally construct a 2^N by 2^N calibration matrix, A, where each row vector corresponds to the measured outcome probabilities of a prepared basis state. In the nominal case of no readout error, A is an identity matrix. With readout error, we can correct the measured counts v_{mea} by minimizing

$$|Av_{\mathrm{cal}} - v_{\mathrm{mea}}|^2 \tag{F1}$$

under the constraint $\sum_j v_{\mathrm{cal},j} = 1$ and $v_{\mathrm{cal},j} \geq 0$. Here v_{cal} is the calibrated counts of v_{mea}. Eq. (F1) can be recasted into a convex optimization problem and solved by quadratic programming using packages such as CVXOPT [52]. The overhead for measuring A and minimizing Eq. (F1) increases exponentially with N. We modify this calibration procedure to have a scalable way to perform readout correction using two key features of the MQC method. For one, we only need to measure the probability that the sate is in $|000..00\rangle$. Two, we expect that the MQC output for imperfections in the GHZ state to result in low excitation states.

This is not entirely unexpected since for an ideal GHZ state, the MQC output has only two distinct states: $|000..00\rangle$ and $|100..00\rangle$. With an imperfect GHZ state and readout errors we expect the output counts to spread out but stay within the low excitation manifolds. Combining these two features we can significantly reduce the overhead for readout calibration by truncating A to only correct for states with significant weights. For example, we can reasonably conclude that the final measurement will not include states such as $|111..11\rangle$. Our metric to verify GHZ entanglement requires MQC amplitudes I_0 and I_N. In FIG. 7**A** we plot the corrected I_0 and I_N as a function of the number of states used in the truncated A matrix (call it A_t); we see a rapid convergence after just 32 states. Interestingly, I_0 decreases as we add more states into the readout calibration, while I_N is relatively unchanged. While keeping such a low number of states may not be sufficient to correct for the entire output vector, it is sufficient to accurately correct for the $|000..00\rangle$ state. In FIG. 7**B** we compare all counts and the largest 256 counts from all experiments for each N.

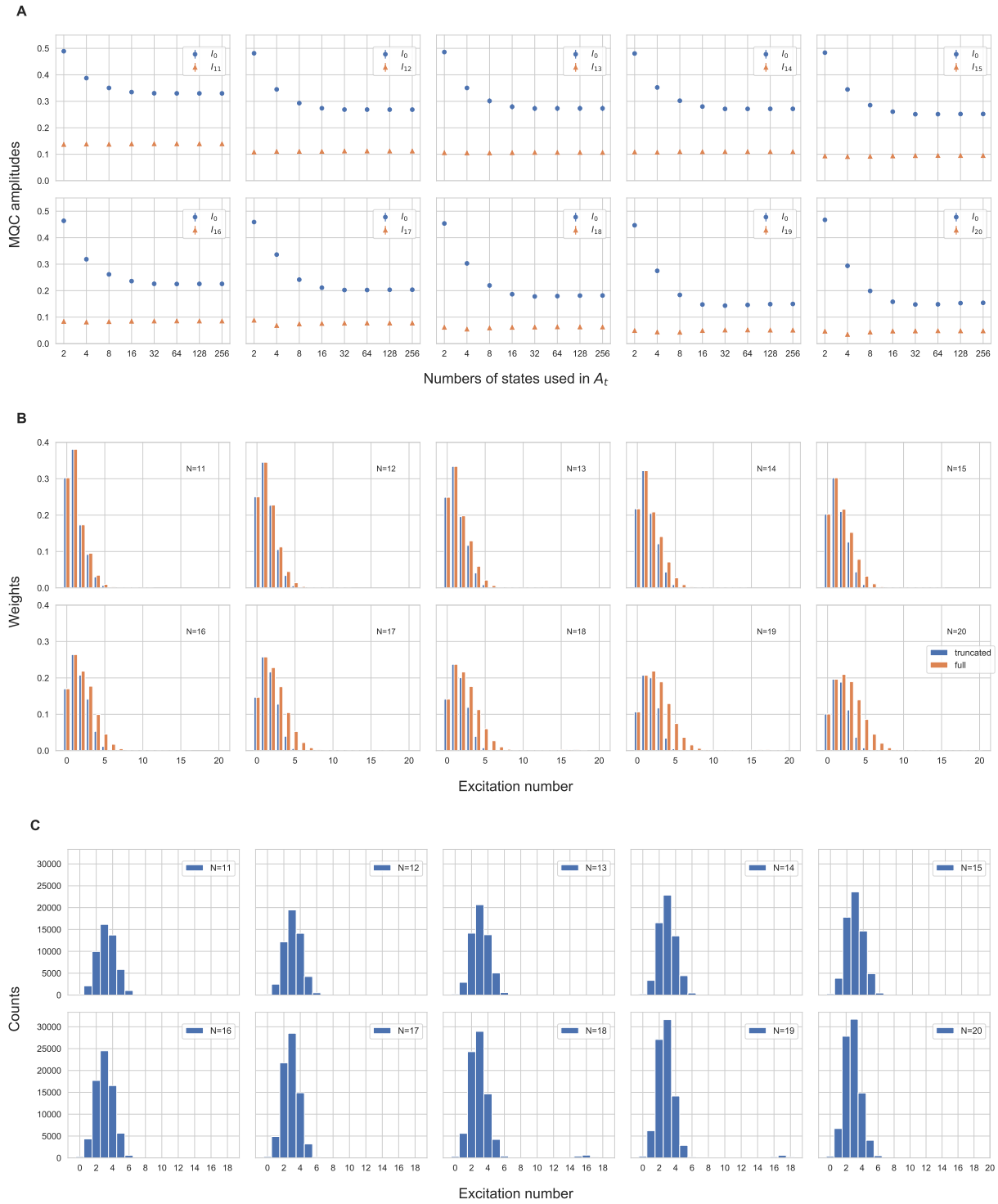

FIG. 7. **Additional data for N = 11 to N = 20 MQC experiments A**: readout corrected MQC amplitudes I_0 and I_N as a function of the number of states used in A_t. **B**: the largest 256 counts and full counts for each N are plotted as a function of excitation number. The full counts are normalized such that the sum over all excitation is one. **C**: the histogram of excitation number is plotted using the largest 256 counts from all experiments for each N. Interestingly, three excitation states have the highest probability for all N.

The counts are grouped according to excitation number (number of ones) and divided by the total number of counts. For small N, there is little difference between all counts and the largest 256 counts, indicating most of

the weight in the output are contained in the largest 256 counts. As N increases however, the total counts begins to spread out to higher excitation numbers, while the largest 256 counts are still localized in the low excitation numbers. This discrepancy however does not affect the calibrated values of the all zeroes count, as demonstrated by the convergence of MQC amplitudes. In addition, the largest 256 states all have similar excitation distributions centered around three excitations independent of N, as shown in FIG. 7**C**. This suggests the readout calibration based on A_t is scalable for measuring MQC amplitudes in GHZ states.

The truncated A matrix cannot correct readout errors from parity oscillation experiments, since the output counts will be distributed across all eigenstates. An alternative to scalable readout calibration is to approximate the full A matrix as a tensor product of A matrices of each qubit [17, 20], this approach is valid when there is little to no readout cross-talk between qubits.

[1] P. Shor, Proc. 37nd Annual Symposium on Foundations of Computer Science , 56 (1996).
[2] S. Bravyi, D. Gosset, and R. König, Science **362**, 308 (2018).
[3] J. Preskill, Quantum **2**, 79 (2018).
[4] E. Knill, D. Leibfried, R. Reichle, J. Britton, R. B. Blakestad, J. D. Jost, C. Langer, R. Ozeri, S. Seidelin, and D. J. Wineland, Phys. Rev. A **77**, 012307 (2008).
[5] E. Magesan, J. M. Gambetta, and J. Emerson, Phys. Rev. A **85**, 042311 (2012).
[6] E. Magesan, J. M. Gambetta, B. R. Johnson, C. A. Ryan, J. M. Chow, S. T. Merkel, M. P. da Silva, G. A. Keefe, M. B. Rothwell, T. A. Ohki, M. B. Ketchen, and M. Steffen, Phys. Rev. Lett. **109**, 080505 (2012).
[7] S. Sheldon, L. S. Bishop, E. Magesan, S. Filipp, J. M. Chow, and J. M. Gambetta, Phys. Rev. A **93**, 012301 (2016).
[8] S. Flammia and Y.-K. Liu, Phys. Rev. Lett. **106**, 230501 (2011).
[9] M. P. da Silva, O. Landon-Cardinal, and D. Poulin, Phys. Rev. Lett. **107**, 210404 (2011).
[10] D. C. McKay, S. Sheldon, J. A. Smolin, J. M. Chow, and J. M. Gambetta, arXiv preprint **arXiv:1712.06550** (2017).
[11] T. J. Proctor, A. Carignan-Dugas, K. Rudinger, E. Nielsen, R. Blume-Kohout, and K. Young, arXiv e-prints (2018), arXiv:1807.07975 [quant-ph].
[12] A. W. Cross, L. S. Bishop, S. Sheldon, P. D. Nation, and J. M. Gambetta, arXiv e-prints (2018), arXiv:1811.12926 [quant-ph].
[13] Y. Wang, Y. Li, Z.-q. Yin, and B. Zeng, npj Quantum Information **4**, 46 (2018).
[14] G. J. Mooney, C. D. Hill, and L. C. L. Hollenberg, arXiv e-prints (2019), arXiv:1903.11747 [quant-ph].
[15] P. Shor, SIAM Journal on Computing **26**, 1484 (1997), https://doi.org/10.1137/S0097539795293172.
[16] R. Raussendorf and H. J. Briegel, Phys. Rev. Lett. **86**, 5188 (2001).
[17] C. Song, K. Xu, W. Liu, C. ping Yang, S.-B. Zheng, H. Deng, Q. Xie, K. Huang, Q. Guo, L. Zhang, P. Zhang, D. Xu, D. Zheng, X. Zhu, H. Wang, Y.-A. Chen, C.-Y. Lu, S. Han, and J.-W. Pan, Phys. Rev. Lett. **119**, 180511 (2017).
[18] T. Monz, P. Schindler, J. T. Barreiro, M. Chwalla, D. Nigg, W. A. Coish, M. Harlander, W. Hänsel, M. Hennrich, and R. Blatt, Phys. Rev. Lett. **106**, 130506 (2011).
[19] X.-L. Wang, Y.-H. Luo, H.-L. Huang, M.-C. Chen, Z.-E. Su, C. Liu, C. Chen, W. Li, Y.-Q. Fang, X. Jiang, J. Zhang, L. Li, N.-L. Liu, C.-Y. Lu, and J.-W. Pan, Phys. Rev. Lett. **120**, 260502 (2018).
[20] M. Gong, M.-C. Chen, Y. Zheng, S. Wang, C. Zha, H. Deng, Z. Yan, H. Rong, Y. Wu, S. Li, F. Chen, Y. Zhao, F. Liang, J. Lin, Y. Xu, C. Guo, L. Sun, A. D. Castellano, H. Wang, C. Peng, C.-Y. Lu, X. Zhu, and J.-W. Pan, Phys. Rev. Lett. **122**, 110501 (2019).
[21] C. Song, K. Xu, H. Li, Y. Zhang, X. Zhang, W. Liu, Q. Guo, Z. Wang, W. Ren, J. Hao, H. Feng, H. Fan, D. Zheng, D. Wang, H. Wang, and S. Zhu, Observation of multi-component atomic schrdinger cat states of up to 20 qubits (2019), arXiv:1905.00320.
[22] A. Omran, H. Levine, A. Keesling, G. Semeghini, T. T. Wang, S. Ebadi, H. Bernien, A. S. Zibrov, H. Pichler, S. Choi, J. Cui, M. Rossignolo, P. Rembold, S. Montangero, T. Calarco, M. Endres, M. Greiner, V. Vuleti, and M. D. Lukin, Generation and manipulation of schrdinger cat states in rydberg atom arrays (2019), arXiv:1905.05721.
[23] C. L. Degen, F. Reinhard, and P. Cappellaro, Rev. Mod. Phys. **89**, 035002 (2017).
[24] J. M. Chow, A. D. Córcoles, J. M. Gambetta, C. Rigetti, B. R. Johnson, J. A. Smolin, J. R. Rozen, G. A. Keefe, M. B. Rothwell, M. B. Ketchen, and M. Steffen, Physical Review Letters **107**, 080502 (2011).
[25] C. Rigetti and M. Devoret, Phys. Rev. B **81**, 134507 (2010).
[26] S. Sheldon, E. Magesan, J. M. Chow, and J. M. Gambetta, Phys. Rev. A **93**, 060302 (2016).
[27] Cramming more power into a quantum device, `https://www.ibm.com/blogs/research/2019/03/power-quantum-device/`, accessed: 2019-03-04.
[28] D. C. McKay, C. J. Wood, S. Sheldon, J. M. Chow, and J. M. Gambetta, Phys. Rev. A **96**, 022330 (2017).
[29] J. Baum, M. Munowitz, A. N. Garroway, and A. Pines, The Journal of Chemical Physics **83**, 2015 (1985), https://doi.org/10.1063/1.449344.
[30] K. X. Wei, C. Ramanathan, and P. Cappellaro, Phys. Rev. Lett. **120**, 070501 (2018).
[31] M. Gärttner, J. G. Bohnet, A. Safavi-Naini, M. L. Wall, J. J. Bollinger, and A. M. Rey, Nature Physics **13**, 781 EP (2017), article.
[32] P. Cappellaro, J. Emerson, N. Boulant, C. Ramanathan, S. Lloyd, and D. G. Cory, Phys. Rev. Lett. **94**, 020502 (2005).
[33] J. J. Bollinger, W. M. Itano, D. J. Wineland, and D. J. Heinzen, Phys. Rev. A **54**, R4649 (1996).
[34] D. Leibfried, M. D. Barrett, T. Schaetz, J. Britton, J. Chiaverini, W. M. Itano, J. D. Jost, C. Langer, and D. J. Wineland, Science **304**, 1476 (2004).

[35] V. Giovannetti, S. Lloyd, and L. Maccone, Science **306**, 1330 (2004).

[36] M. Gärttner, P. Hauke, and A. M. Rey, Phys. Rev. Lett. **120**, 040402 (2018).

[37] O. Ghne and G. Tth, Physics Reports **474**, 1 (2009).

[38] O. Ghne and M. Seevinck, New Journal of Physics **12**, 053002 (2010).

[39] C. A. Sackett, D. Kielpinski, B. E. King, C. Langer, V. Meyer, C. J. Myatt, M. Rowe, Q. A. Turchette, W. M. Itano, D. J. Wineland, and C. Monroe, Nature **404**, 256 EP (2000).

[40] D. Leibfried, E. Knill, S. Seidelin, J. Britton, R. B. Blakestad, J. Chiaverini, D. B. Hume, W. M. Itano, J. D. Jost, C. Langer, R. Ozeri, R. Reichle, and D. J. Wineland, Nature **438**, 639 EP (2005).

[41] E. L. Hahn, Phys. Rev. **80**, 580 (1950).

[42] D. Cruz, R. Fournier, F. Gremion, A. Jeannerot, K. Komagata, T. Tosic, J. Thiesbrummel, C. L. Chan, N. Macris, M.-A. Dupertuis, and C. Javerzac-Galy, arXiv e-prints (2018), arXiv:1807.05572 [quant-ph].

[43] G. Aleksandrowicz, T. Alexander, P. Barkoutsos, L. Bello, Y. Ben-Haim, D. Bucher, F. J. Cabrera-Hernádez, J. Carballo-Franquis, A. Chen, C.-F. Chen, J. M. Chow, A. D. Córcoles-Gonzales, A. J. Cross, A. Cross, J. Cruz-Benito, C. Culver, S. D. L. P. González, E. D. L. Torre, D. Ding, E. Dumitrescu, I. Duran, P. Eendebak, M. Everitt, I. F. Sertage, A. Frisch, A. Fuhrer, J. Gambetta, B. G. Gago, J. Gomez-Mosquera, D. Greenberg, I. Hamamura, V. Havlicek, J. Hellmers, Ł. Herok, H. Horii, S. Hu, T. Imamichi, T. Itoko, A. Javadi-Abhari, N. Kanazawa, A. Karazeev, K. Krsulich, P. Liu, Y. Luh, Y. Maeng, M. Marques, F. J. Martín-Fernández, D. T. McClure, D. McKay, S. Meesala, A. Mezzacapo, N. Moll, D. M. Rodríguez, G. Nannicini, P. Nation, P. Ollitrault, L. J. O'Riordan, H. Paik, J. Pérez, A. Phan, M. Pistoia, V. Prutyanov, M. Reuter, J. Rice, A. R. Davila, R. H. P. Rudy, M. Ryu, N. Sathaye, C. Schnabel, E. Schoute, K. Setia, Y. Shi, A. Silva, Y. Siraichi, S. Sivarajah, J. A. Smolin, M. Soeken, H. Takahashi, I. Tavernelli, C. Taylor, P. Taylour, K. Trabing, M. Treinish, W. Turner, D. Vogt-Lee, C. Vuillot, J. A. Wildstrom, J. Wilson, E. Winston, C. Wood, S. Wood, S. Wörner, I. Y. Akhalwaya, and C. Zoufal, Qiskit: An open-source framework for quantum computing (2019).

[44] J. A. Smolin, J. M. Gambetta, and G. Smith, Phys. Rev. Lett. **108**, 070502 (2012).

[45] M. Hein, J. Eisert, and H. J. Briegel, Phys. Rev. A **69**, 062311 (2004).

[46] H. Kaufmann, T. Ruster, C. T. Schmiegelow, M. A. Luda, V. Kaushal, J. Schulz, D. von Lindenfels, F. Schmidt-Kaler, and U. G. Poschinger, Phys. Rev. Lett. **119**, 150503 (2017).

[47] M. Takita, A. W. Cross, A. D. Córcoles, J. M. Chow, and J. M. Gambetta, Phys. Rev. Lett. **119**, 180501 (2017).

[48] A. Ozaeta and P. L. McMahon, Quantum Science and Technology **4**, 025015 (2019).

[49] K. Temme, S. Bravyi, and J. M. Gambetta, Phys. Rev. Lett. **119**, 180509 (2017).

[50] A. Kandala, K. Temme, A. D. Córcoles, A. Mezzacapo, J. M. Chow, and J. M. Gambetta, Nature **567**, 491 (2019).

[51] D. C. McKay, S. Sheldon, J. A. Smolin, J. M. Chow, and J. M. Gambetta (2017), arXiv:1712.06550.

[52] M. S. Anderson, J. Dahl, and L. Vandenberghe, CVXOPT: A python package for convex optimization, version 1.2.3, `https://cvxopt.org/` (2019).